nature portfolio

https://doi.org/10.1038/s41565-021-00884-6

Supplementary information

Observation of superdiffusive phonon transport in aligned atomic chains

In the format provided by the authors and unedited

Supplementary Material for

"**Observation of superdiffusive phonon transport in aligned atomic chains**"

Lin Yang,[1] Yi Tao,[1,2] Yanglin Zhu,[3] Manira Akter,[4] Ke Wang,[5] Zhiliang Pan,[1] Yang Zhao,[1] Qian Zhang,[1] Yaqiong Xu,[6,7] Renkun Chen,[8] Terry T. Xu,[4] Yunfei Chen,[2] Zhiqiang Mao,[3] and Deyu Li[1,*]

[1]Department of Mechanical Engineering, Vanderbilt University, Nashville, TN 14, USA.

[2]School of Mechanical Engineering and Jiangsu Key Laboratory for Design and Manufacture of Micro-Nano Biomedical Instruments, Southeast University, Nanjing, 210096, P. R. China.

[3]Department of Physics, Pennsylvania State University, University Park, PA 16802, USA.

[4]Department of Mechanical Engineering and Engineering Science, The University of North Carolina at Charlotte, Charlotte, North Carolina 28223, United States

[5]Materials Research Institute, Pennsylvania State University, University Park, PA 16802, USA

[6]Department of Electrical Engineering and Computer Science, Vanderbilt University, Nashville, TN 37235, USA.

[7]Department of Physics and Astronomy, Vanderbilt University, Nashville, TN 37235, USA.

[8]Department of Mechanical and Aerospace Engineering, University of California-San Diego, La Jolla, CA, 92093, USA

*Correspondence to: deyu.li@vanderbilt.edu

Contents

Supplementary Note 1. Sample preparation and cross-section characterization

Single crystals of $NbSe_3$ were grown by the chemical vapor transport (CVT) method, and the detailed growth condition can be found elsewhere[1]. Owing to the anisotropic bonding strengths along different crystalline directions, the as-grown bulk crystals appear to have a fibroid nature with millimeter length along the axial direction. In general, the smallest dimension is along the *a* axis, while the intermediate one is along the *c* axis. The weak inter-chain bonding strengths allow for easy cleavages along the *bc* and *ab* plane (Fig. 1a-b in the main paper)[2]. We obtained thin $NbSe_3$ nanowires by a liquid exfoliation method[1,3], in which we first dispersed bulk crystals of $NbSe_3$ into reagent alcohol, and sonicated for 3 hours. The resulting mixture contains $NbSe_3$ nanowires with different lateral dimensions and lengths. We then drop-casted the solution onto the surface of a piece of polydimethylsiloxane (PDMS) for subsequent transfer of individual nanowires to measurement devices with a custom-built micromanipulator[4].

Note that as the intra-chain covalent bonds are much stronger than the inter-chain van der Waals (vdW) interactions, the nanowires are cleaved along the vdW planes during sonication, and all resulting $NbSe_3$ nanowire samples are oriented along the same intra-chain *b* axis. This has been confirmed by high resolution transmission electron microscopy (HRTEM) studies. Selected area electron diffraction (SAED) patterns were recorded for 17 $NbSe_3$ nanowires with different hydraulic diameters, D_h, and the results for two representative nanowires with D_h of 67.9 nm and 10.7 nm are shown in Fig. S1, which confirm that the nanowires of different diameters are oriented along the *b* axis direction.

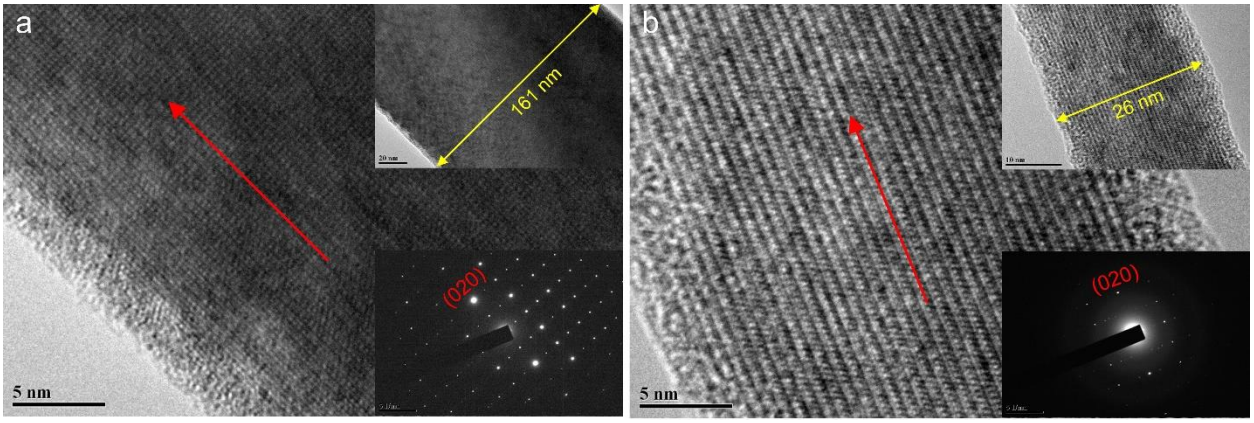

Supplementary Figure 1. (a) HRTEM image of a 161 nm wide, 43 nm thick (D_h = 67.9 nm) $NbSe_3$ nanowire, where the selected area electron diffraction (SAED) pattern recorded at the zone axis of [100] shows that the crystalline orientation is along <010> direction, *i.e.*, *b* axis. (b) HRTEM image of a 26 nm wide, 6.7 nm thick (D_h = 10.7 nm) $NbSe_3$ nanowire, and the SAED pattern recorded at the zone axis of [100] also confirms that the crystalline orientation is along <010> direction.

Different from nanowires synthesized directly by chemical vapor deposition, the cross-sections of the exfoliated quasi-1D vdW nanowires tend to be of irregular shapes. As such, it is necessary to obtain the exact cross-sectional area of each tested sample to accurately extract the thermal/electrical conductivity. For $NbSe_3$ nanowires with relatively large lateral dimensions, we used focused ion beam to directly cut open the cross-sections, and the detailed procedures can be found in our recent reports[1,3]. Fig. S2a is a high resolution scanning electron microscopy (HRSEM)

image of a $NbSe_3$ nanowire of 22 nm thick. Note that this nanowire was not placed with the wider lateral dimension facing the substrate. To confirm the results, we also placed another segment of the same nanowire on a flat Si substrate and performed atomic force microscopy (AFM) characterization. The obtained result is shown in Fig. S2b, where the obtained thickness is 23 nm, very close to what we measured from the HRSEM image. Fig. S2c,d show the SEM and AFM images of a thinner nanowire.

For ultra-thin $NbSe_3$ nanowires, we obtain the thickness data by AFM scanning, width from SEM imaging, and approximate the cross-section to be of rectangular shape. As these two dimensions are projections toward the width and height of a rectangle, the obtained data represents an overestimation of the cross-sectional area; and the actual thermal conductivity of the nanowire will only be higher than the values shown in Fig. 2a. Importantly, for the length dependence study, to ensure the best control, we re-suspended the same nanowire sample multiple times with different lengths bridging the two membranes so the uncertainty in the cross-sectional area represents a systematic error that will not alter the trend.

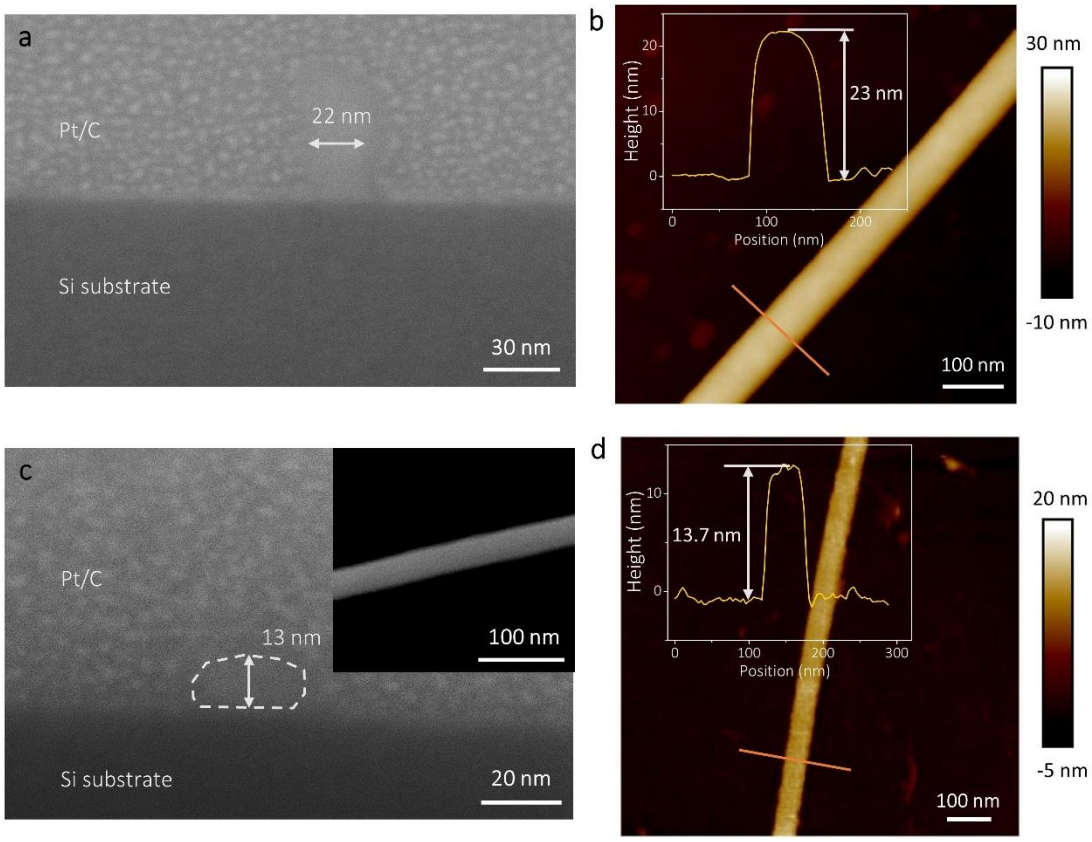

Supplementary Figure 2. (a) HRSEM micrograph of the cross-section of a 30.2 nm diameter $NbSe_3$ nanowire after cutting open the cross-section, where the nanowire was placed on a Si substrate and wrapped by a thick film of Pt/C composite prepared by electron beam induced deposition (EBID). (b) AFM scanning result of another segment of the same nanowire as in (a). (c-d) HRSEM image showing the cross-section of a 18.9 nm diameter $NbSe_3$ nanowire and the AFM scanning result of the same wire.

Supplementary Note 2. Cross-section uniformity examination

As described above, the $NbSe_3$ nanowires are prepared using liquid exfoliation. To confirm that the wires are uniform, we examined the wire cross-section at different locations along the axial direction of the as-fabricated $NbSe_3$ nanowires. This helps us rule out the possibility of variations of the cross-section and further confirm the size and length dependence for the measured thermal conductivity.

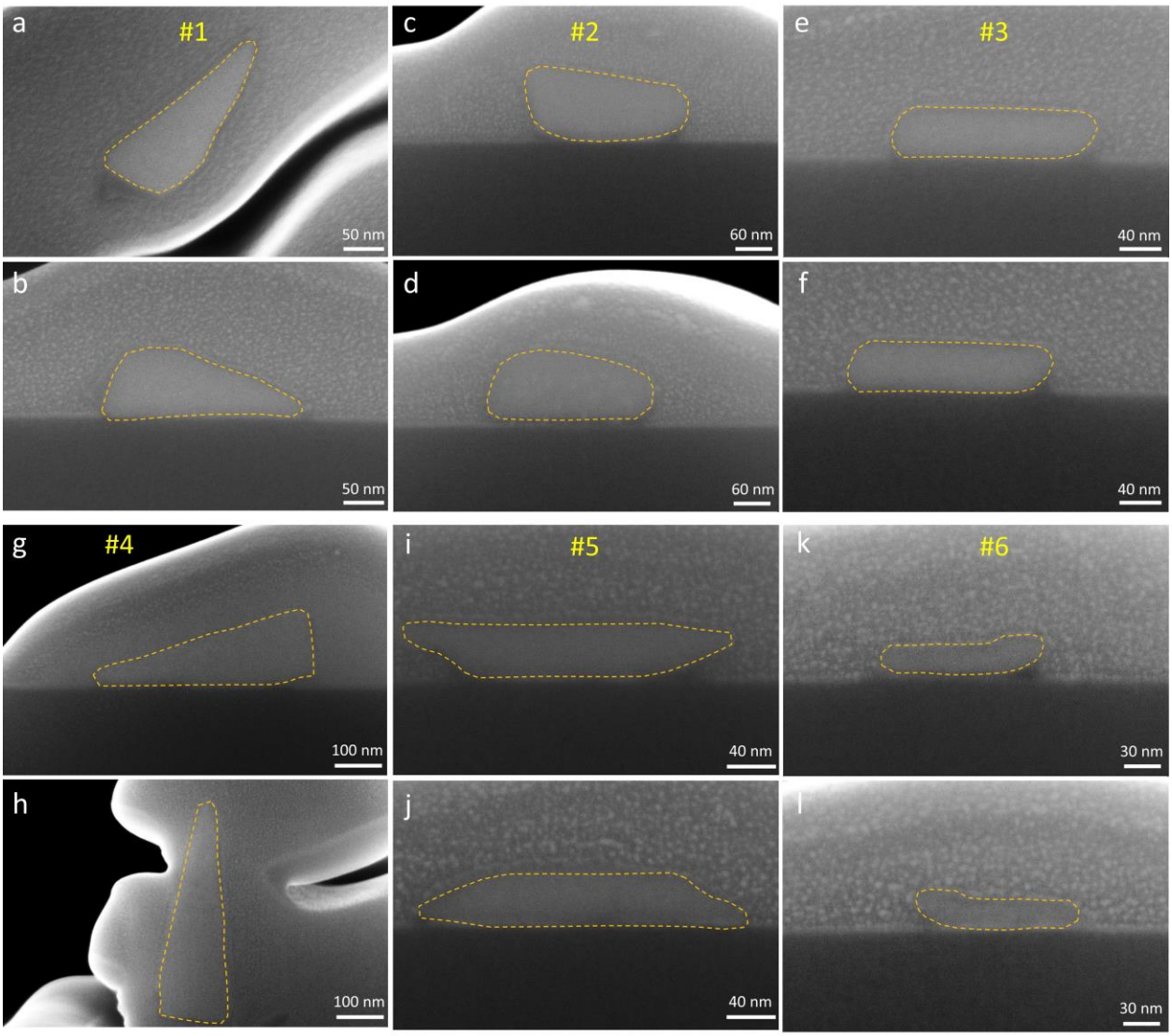

Supplementary Figure 3. SEM images showing the cross-section at the two ends of six $NbSe_3$ nanowires. Sample #1 (a-b), #2 (c-d), #3 (e-f), #4 (g-h), #5 (i-j), and #6 (k-l).

To do so, we randomly picked six long nanowires (>15 μm), and cut off two segments at the two ends of each nanowire. After transferring the wire segments to a flat Si substrate, the cross-section of the nanowires are cut open and examined by SEM. Fig. S3 shows the comparison of the cross-section at the two ends of the same nanowire for the six examined nanowires. It is important to note that the same dashed line contour is used to outline the cross-section for the same nanowire, where a good agreement could be observed for the two segments. To further show the uniformity,

we measured the exact cross-sectional area and perimeter for each segments, and the results are summarized in Table S1 below. It can be seen that the calculated hydraulic diameter agrees very well for the examined two segments, with < 4% difference. The observed difference is less than the 10% error assumed for the cross-sectional area in our uncertainty analysis.

For nanowires with smaller cross-sections, the boundary of the cross-section becomes less discernable in the SEM images. As such, we performed AFM scanning for the entire nanowire, and compared the cross-section profiles at the two ends and a middle part of the same nanowire. Fig. S4 shows the height contour and cross-section profiles obtained from AFM. For all of three nanowires tested this way, it can be seen that the cross-section profiles are very similar along the axial direction with length over ~15 μm, and the thickness difference is within ~5% of the average thickness. This again verifies that the cross-sections are very uniform for wires with very small transverse dimensions.

Supplementary Table 1. Summary of the measured perimeter, cross-sectional area, and the calculated hydraulic diameter at the two ends of the same nanowire for six nanowires.

sample	Segment #1			Segment #2		
	Perimeter (nm)	Area (nm^2)	Hydraulic diameter (nm)	Perimeter (nm)	Area (nm^2)	Hydraulic diameter (nm)
#1	584	15988	110	582	15796	109
#2	634	23078	146	616	21953	143
#3	449	8917	79	440	8628	78
#4	1139	48820	171	1104	49045	178
#5	549	10515	77	542	9972	74
#6	312	3065	39	310	3173	41

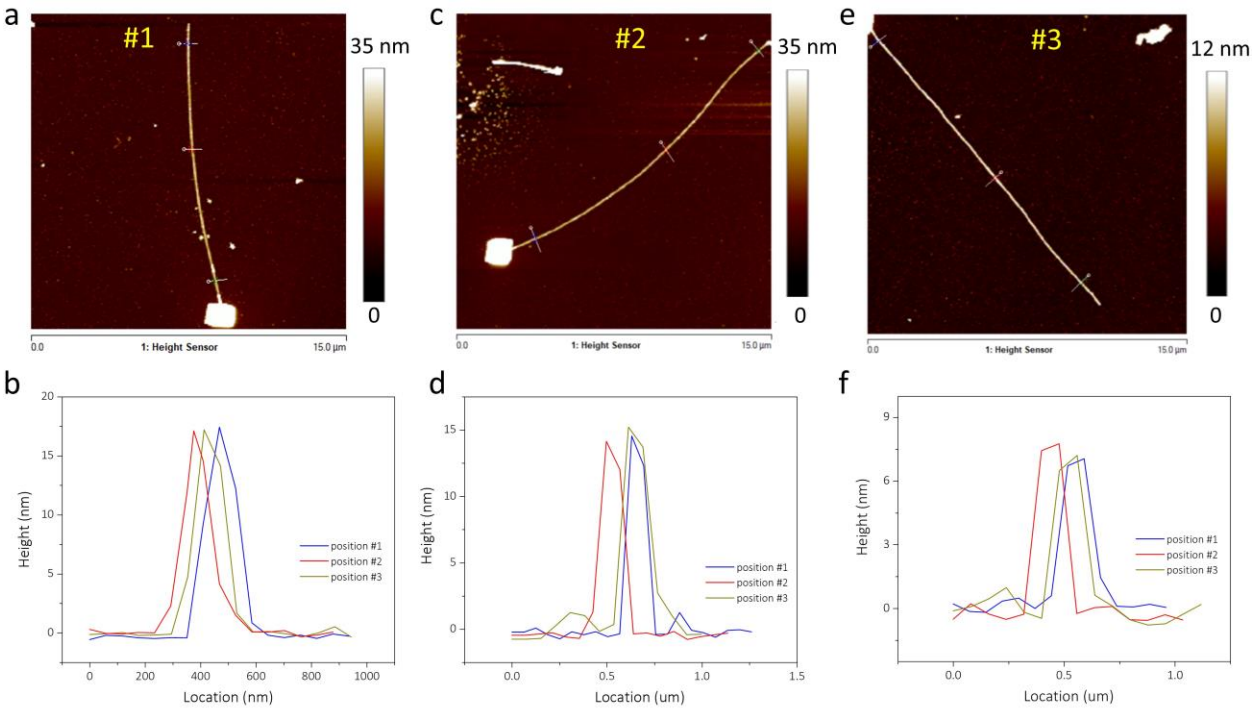

Supplementary Figure 4. AFM images and the cross-section profiles at the two ends and a middle point of the same $NbSe_3$ nanowire for sample #1 (a-b), #2 (c-d), and #3 (e-f).

Supplementary Note 3. Thermal conductance measurement sensitivity characterization

We conducted thermal and electrical measurements in a cryostat (Janis CCS-400/204) operated under a high vacuum (<1 × 10^{-6} mbar) with dual radiation shields installed. For thermal conductivity measurement, we measured the temperatures of the heating and sensing membranes through monitoring the electrical resistance of the platinum (Pt) thermometers. The Joule heating generated by the DC current on the heating membrane is calculated based on the measured current using a current preamplifier and the measured electrical resistance of the Pt heater, and the heat flux, q, transported through the nanowire sample to the sensing membrane is calculated based on constructing the thermal model for the suspended microdevice[5]. Then, the thermal conductivity is calculated according to $\kappa = qL/A\Delta T$, where L is the suspended sample length, A is cross-sectional area, and ΔT is the temperature difference between the heating and sensing membranes.

For the traditional 4-point *I-V* measurement approach using the suspended microdevice, the sensitivity of the thermal conductance measurement is ~0.3-0.5 nW/K, which is mainly limited by two factors: i) long period temperature drifts of the proportional-integral-derivative (PID) controlled temperature stage (~100 mK), and ii) the lock-in amplifier noise due to the large dynamic reserve required to measure small voltage changes on top of a large output voltage[6]. With implementation of the Wheatstone bridge scheme at the sensing side of the suspended microdevice, the measurement sensitivity could be as small as ~10 pW/K[6].

In this work, we choose a bridge driving voltage v_s = 20 mV, and the sensitivity, time constant as well as the filter roll-off settings of the lock-in amplifier (Stanford Research SR830) are set to be 50 μV, 1 s and 24 dB/oct, respectively. The parameters adopted here are chosen based on our

practice for sensitive measurement in a large temperature range and reasonable data acquisition time. In order to characterize the measurement sensitivity, we monitored the bridge output voltage v_g for two hours with the temperature controller set at 300 K. Fig. S5 plots the sensing side temperature fluctuations as a function of time, which also represents the noise equivalent temperature fluctuation, *NET*. It can be seen that the temperature fluctuation measured by the bridge scheme is below 5 mK, which is much lower than that of the 4-point method, 13-27 mK at 300 K[6].

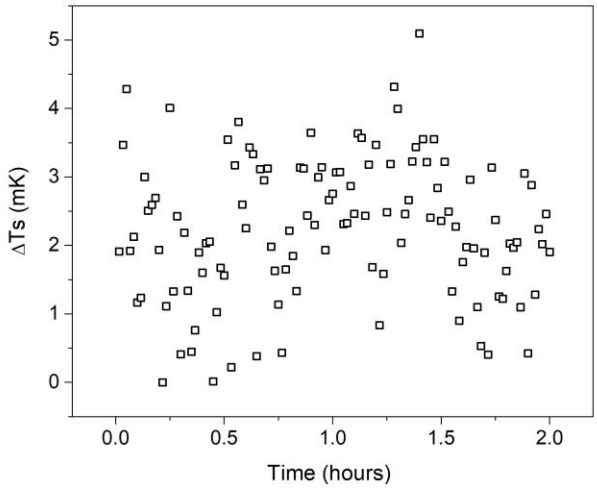

Supplementary Figure 5. The monitored temperature fluctuation of the sensing side membrane with the Wheatstone bridge scheme in 2 hours at 300 K.

If we take the *NET* as 4 mK, a noise equivalent conductance NEG_s could be calculated. To do this, we use the measured thermal conductance of the SiNx beams (G_b) at 300 K (73 nW/K), and the calculated temperature difference between the heating and sensing membranes as 8 K,

$$NEG_s = G_b \frac{NET}{\Delta T_h - \Delta T_s} \approx 73 \text{ nW/K} \times \frac{4 \text{ mK}}{8 \text{ K}} = 0.036 \text{ nW/K}. \quad \text{(S1)}$$

Here ΔT_h and ΔT_s are the temperature changes of the heating and sensing membranes, respectively. The obtained NEG_s is a little higher than that achieved by Wingert et al. (~ 10 pW/K), which could be attributed to the larger bridge driving voltage, v_s = 100 mV and a smaller sensitivity of 5 μV adopted in their experimental settings[6]. The noise induced electrical resistance fluctuation ΔR_s can be expressed as[6]:

$$\Delta R_s = \frac{\Delta v_g}{v_s} \frac{\left(R_s + R_2\right)^2}{R_2}. \quad \text{(S2)}$$

Here Δv_g is bridge voltage noise, R_s is sensing side membrane resistance, and R_2 is the outside resistance paired with R_s in the bridge circuit [6]. Therefore, increasing v_s leads to a smaller ΔR_s, and as $NET = \Delta R_s / R_s / TCR$, this would result in a smaller temperature fluctuation. However, raising the driving voltage v_s could lead to unwanted heating and unbalanced base temperature rise of the heating and sensing membranes[7]. As such, we choose a smaller bridge driving voltage of 20 mV. As the obtained NEG_s is still much smaller than the measured lowest sample intrinsic thermal

conductance (0.18 nW/K), this should allow us to perform thermal conductivity measurements with good accuracy.

Supplementary Note 4. Radiation heat loss from sample surface

Owing to the radiation heat loss from the sample surface to the surroundings, the heat flux received by the sensing side membrane is always smaller than that transmitted from the heating side, and for the same aspect ratio, the radiation heat loss will increase with increasing nanowire length. As such, we need to carefully estimate the radiation heat loss for thin $NbSe_3$ nanowire samples with ultra-long suspended length.

According to the thermal fin model, the thermal resistance of the nanowire after considering the radiation heat loss from the circumference could be expressed as[8]:

$$R_s = \frac{1}{\sqrt{\pi^2 \varepsilon \sigma \kappa T^3 d^3}} \frac{\sinh \beta L}{\cosh \beta L}, \tag{S3}$$

where $\beta = \sqrt{4\varepsilon\sigma T^3 P/\kappa A}$, ε, σ, κ, T, d, P, A, and L are the surface emissivity, Stefan-Boltzmann constant, thermal conductivity, temperature, diameter, perimeter, cross-sectional area and length of the $NbSe_3$ nanowire, respectively. For $\beta L \ll 1$, the thermal resistance is reduced to the nanowire conduction thermal resistance:

$$R_s = \frac{L}{\kappa A}. \tag{S4}$$

Therefore, the relative error in neglecting the radiation heat loss is

$$\Delta = \frac{\beta L \cosh \beta L}{\sinh \beta L} - 1. \tag{S5}$$

As the surface emissivity of $NbSe_3$ is not readily available, we take ε =1 in the calculation, which represents an overestimation for the relative error. For the thinnest $NbSe_3$ nanowire sample measured in this work with the largest surface area to volume ratio (D_h = 6.8 nm, L = 30 μm), the calculated error is only ~1%, and thus the radiation heat loss is not important for the long thin nanowire samples examined in this work.

Supplementary Note 5. Thermal conductivity measurement uncertainty

Thermal conductivity measurement uncertainty comes from several error sources, namely, the uncertainty in the extracted thermal conductance and the errors related to the sample dimension. The thermal conductivity of the nanowire sample is calculated as $\kappa = GL/A$, where G is the measured sample thermal conductance, L is the suspended wire length between the two membranes, and A is the cross-sectional area of the measured sample. Following the error propagation rule to estimate the overall measurement uncertainty for the extracted thermal conductivity, the relative uncertainty of κ can be written as

$$\frac{\delta\kappa}{\kappa}=\sqrt{\left(\frac{\delta G}{G}\right)^2+\left(\frac{\delta L}{L}\right)^2+\left(\frac{\delta A}{A}\right)^2}\ . \tag{S6}$$

The uncertainty of the measured thermal conductance $\delta G/G$ mainly comes from the electrical measurements, which is evaluated based on a Monte Carlo method that has been described in our previous work[9]. Using this method, $\delta G/G$ is estimated to be 2~3% depending on the temperature.

The length L is measured by SEM, and the uncertainty is estimated to be 0.2 μm. For relatively large diameter nanowires, the cross-sectional area is obtained from the HRSEM imaging as detailed in Section I, and we conservatively estimated the uncertainty to be less than 10%. For thin nanowires, the thickness of the cross-section is determined from AFM scanning with an error of ~1 nm, and width is from SEM imaging with an error of ~ 2 nm. Based on the uncertainty derived from these sources, the overall uncertainty of the thermal conductivity can be calculated using Eq. (S6), which is determined to be ~11% at 300 K for a 135 nm diameter nanowire, and 26% for the 6.8 nm diameter nanowire at 300 K. It is important to note that as the same nanowire is re-suspended several times for the length dependence measurements, the relatively large uncertainties for the thin nanowires are only for the absolute thermal conductivity value, but not the observed thermal conductivity *versus* length trend in Fig. 2b-c in the manuscript.

Supplementary Note 6. Contact thermal resistance and background thermal conductance subtraction

In experimental studies of thermal transport through nanowires using the microthermal bridge method, the contact thermal resistance between the nanowire sample and the Pt electrodes on the suspended membranes has to be carefully considered. We have previously shown that for $NbSe_3$ nanowires, EBID of Pt/C at the contacts between the nanowire and Pt electrodes using a dual-beam system (FIB/SEM, FEI Helios NanoLab G3) can minimize the contact thermal resistance by enlarging the contact area and reduce the contact thermal resistance to a negligible level[1]. However, to measure the length dependence of the thermal conductivity, we need to re-suspend the same nanowire sample multiple times so we cannot do the EBID treatment. Luckily, the vdW interactions between the nanowire sample and the suspended membranes naturally lead to a contact between a flat surface of the wire and the Pt electrodes; and the relatively large contact area between two flat surfaces results in a marginal contact thermal resistance as compared to the intrinsic resistance of the $NbSe_3$ nanowires. In fact, we have previously shown that for thin ribbon-like nanowires (silicon nanoribbons), the large contact area between the flat ribbon surface and the suspended membrane renders the contact thermal resistance negligible as compared to the resistance of the nanowire itself[10].

It is well-known that the length dependence of thermal conductivity can be induced by either the comparable phonon mean free path and sample length, or significant thermal resistance at the contact such as that due to limited contact area between a circular nanowire and the suspended membrane. Luckily, the origin of the length dependence can be distinguished through comparing the thermal conductivity derived from the measured thermal resistance of a specific sample length and that from the differential thermal resistance with respect to sample length.

If the length dependence is due to the contact thermal resistance, then the measured total thermal resistance (R_{tot}) follows a linear trend with length, and the contact thermal resistance can

be extracted through the following relation $R_{tot} = L/\kappa A + R_c$, where L is the sample length between the heat source and heat sink, κ is the intrinsic sample thermal conductivity, A is the sample cross-sectional area, and R_c is the contact thermal resistance. The slope of the resulting linear profile is $1/\kappa A$ with a constant κ that is the intrinsic thermal conductivity of the sample, which is approximately equal to the value extracted from a measurement of a long enough sample where the intrinsic thermal resistance of the nanowire is much larger than that of the contact thermal resistance. This is indeed the case for the 158 nm diameter wire, for which the thermal conductivity converges to a saturated value as the wire length exceeds 7.6 μm, as shown in Fig. 2b in the manuscript.

In our measurements, to probe the length dependence, we realign the same nanowire sample multiple times with different suspended lengths between the two membranes, as shown in Fig. S6a-d for the 158 nm diameter wire. Fig. S6e displays the measured total thermal resistance at 300 K *versus* the suspended length, which indicates that the three data points for L=7.6, 10.8 and 15.3 μm fit into a linear profile perfectly, with the thermal conductivity derived from the slope as 7.34 W/m-K, almost the same as the value of 7.25 W/m-K derived from the measurement with L=15.3 μm. The extracted contact thermal resistance is 6.45×10^5 K/W, which is only 1-3% of the total measured thermal resistance for the samples with a suspended length of 7.6 μm or longer. The measured thermal resistance for the 2.5 μm length sample slightly deviates from the linear profile with a higher value, which is likely due to the fact that the mean free paths of some low frequency phonons are comparable to this small sample length.

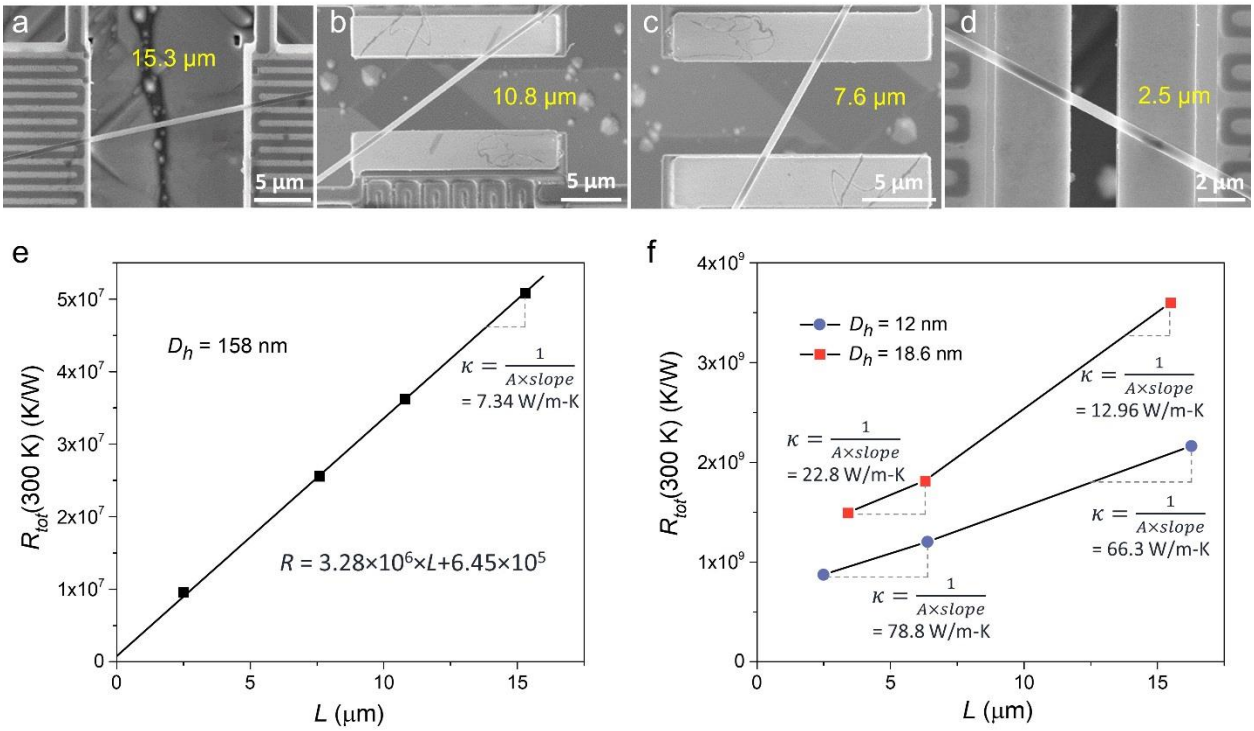

Supplementary Figure 6. (a-d) SEM micrographs of the same 158 nm diameter $NbSe_3$ nanowire re-suspended with four different lengths between the two membranes. (e) Measured room-temperature total thermal resistance *versus* the suspended length for the 158 nm diameter wire, which shows a perfect linear profile for the three data points with L=7.6, 10.8 and 15.3 μm. (f)

Measured room temperature total thermal resistance plotted as a function of the suspended length for the 18.6 and 12 nm diameter wires.

It has been previously shown that for heat transfer between the nanowire and the suspended membranes, a fin model can be used to evaluate the contact thermal resistance, R_c, and the thermalization distance[11,12]. Based on the fin model, the contact thermal resistance between the nanowire and the two membranes can be written as[11,12]:

$$R_c = \frac{2\sqrt{R_{in/L} \cdot R_c''}}{\tanh\left(L_c \sqrt{R_{in/L} / R_c''}\right)}, \quad \text{(S7)}$$

where L_c is the length of the $NbSe_3$ nanowire segment in contact with the membrane, R_c'' is the contact thermal resistance for a unit contact length, and $R_{in/L}$ is the intrinsic nanowire thermal resistance per unit length. When L_c is large enough so that the denominator in Eq. S7 approaches unity, R_c is no longer a function of L_c. In this case, the $NbSe_3$ nanowire is fully thermalized with the supporting membrane. Because the function tanh(x) is already very close to unity for x = 2 (tanh(2) = 0.964), and approaches to unity slowly in an asymptotic manner after $x \geq 2$, we estimated the minimum contact length, $L_{c,min}$, required for the $NbSe_3$ nanowire to be thermalized with the suspended membranes by requiring $L_c\sqrt{R_{in/L}/R_c''} = 2$. With this relation, simple manipulation of Eq. S7 leads to $L_{c,min} \approx R_C/R_{in/L}$. For the 158 nm $NbSe_3$ nanowire as shown in Fig. S6a-d, $R_{in/L}$ is 3.32×10^{12} K/m-W, R_c is extracted to be 6.45×10^5 K/W, and thus $L_{c,min}$ is calculated to be 0.194 μm. This is much less than the contact length of the nanowire with the suspended membranes. In fact, Fig. S6a-d show that the contact length of this $NbSe_3$ nanowire with the suspended membrane are all longer than 3.2 μm. As such, R_c is no longer a function of L_c, and our assumption that R_c remains the same for the same nanowire with different suspended lengths is well justified.

However, if the intrinsic phonon MFP is larger than the nanowire length, then the contact not only poses a constant R_c but also limits the phonon MFP. This is the case for the 18.6 nm and 12 nm diameter wires. In this case, κ becomes length dependent and we cannot extract the contact thermal resistance from the intercept because R_{tot} *versus* L deviates from linear (Fig. S6f), and in the relation, $R_{tot} = L/\kappa A + R_c$, the $L/\kappa A$ term does not disappear as L approaches zero. In fact, when L is very small such that $L \ll MFP$, the transport would be in the fully ballistic regime and the sample intrinsic thermal conductance G would be a constant: $R_{tot} = \frac{1}{G} + R_c$. In this case, the intercepts as L approaching zero would contain both $1/G$ (resistance due the ballistic transport) and R_c (contact thermal resistance in the traditional sense). It is worth noting that while we cannot directly extract the contact thermal resistance for smaller diameter wires, a well-accepted trend is that as the wire becomes thinner, the weight of contact thermal resistance in the total measured resistance reduces. The intrinsic wire thermal resistance is inversely proportional to the square of the wire hydraulic diameter ($R_{in} = L/\kappa A \propto 1/D^2$) while R_c scales inversely with the wire size ($R_c \propto 1/D$, assuming that the contact thermal resistance per unit width remains the same). As such, for the measured total thermal resistance, $R_{tot} = L/\kappa A + R_c$, as D reduces, the increase of R_c is less than that of R_{in}, and R_c/R_{tot} becomes smaller for thinner wires as compared to the value for the 158 nm diameter sample of the same length. For example, we estimate that as the hydraulic diameter of our samples reduces from 158 nm to 6.8 nm, the contact width shrinks from 479 to 18 nm, or by 26 times. This means that the R_c could increase by ~26 times. However, the measured wire resistance (R_{tot}) increases by 43 times as R_{in} is inversely proportional to the square of the

hydraulic diameter, this is the case even though κ of the 6.8 nm diameter wire is ~15 times larger than that of the 158 nm nanowire. As such, the relative contribution of R_c in R_{tot} further drops as the wire diameter shrinks (R_c/R_{tot} is ~1% for the 6.8 nm wire).

While in the normal diffusive transport regime, the intrinsic thermal conductivity can be extracted from the slope of the linear R_{tot} *versus* L curve, as shown in Fig. S6e for the 158 nm diameter sample, if the sample length is comparable to or smaller than the phonon mean free path, the derived thermal conductivity from the slope of the measured R_{tot} *versus* L relation is larger than the value directly calculated from a single measurement with a specific sample length. This is the case for nanowires of < 26 nm diameters. In fact, in the regime where the sample length is much smaller than the phonon mean free path, the measured thermal resistance could become length independent, in this case, the thermal conductivity derived from the slope of the R_{tot} *versus* L line approaches infinity.

As shown in Fig. S6f, for the 18.6 nm diameter wire, the derived thermal conductivity from the two measurements with L=3.4 and 6.3 μm is 22.8 W/m-K, which is much larger than the κ directly derived from the single measurement with L=6.3 μm (8.76 W/m-K). Similarly, the thermal conductivity extracted from the slope of the line segment between the L= 6.3 and 15.5 μm is 12.96 W/m-K, which is again larger than the value directly derived from the measurement with L= 15.5 μm (10.85 W/m-K).

The difference from the thermal conductivities determined from the slope of the line segments between two data points and from the measured thermal resistance at a specific sample length becomes more significant for the 12 nm diameter wire. The calculated thermal conductivity from the slope of the two points (L = 2.5 and 6.4 μm) is 78.8 W/m-K, while the extracted κ from the measurement with L= 6.4 um is 35.3 W/m-K. Similarly, the derived thermal conductivity from the slope of the two points (L = 6.4 and 16.3 μm) is 66.3 W/m-K, while the directly extracted κ from the measurement with L = 16.3 μm is 49.8 W/m-K.

The above facts provide solid evidence that the length dependence observed for wires of < 26 nm diameter is due to superdiffusive phonon transport and cannot be attributed to the effects of contact thermal resistance.

The scaling between the contact thermal resistance and wire intrinsic resistance also suggest that the observed linear increase of the temperature dependence of the thermal conductivity is not due to the contact thermal resistance. As discussed above, we can extract the contact thermal resistance from linear fitting of the measured total thermal resistance *versus* the sample length for the 158 nm diameter wire, and the weight of the contact thermal resistance in the measured total thermal resistance with a sample length of 15.3 μm in the temperature range of 100 to 300 K is shown in Fig. S7. It can be seen that the contact thermal resistance only contributes to 1-3% of the total measured thermal resistance in this temperature range. As the weight of the contact thermal resistance in the total measured resistance gets smaller for thinner wires, the effects of contact thermal resistance contribution should be even less important as the hydraulic diameter reduces; and therefore, the observed thermal conductivity increase with temperature for thinner wires in the upper panel of Fig. 2d cannot be induced by the < 3% weight of the contact thermal resistance.

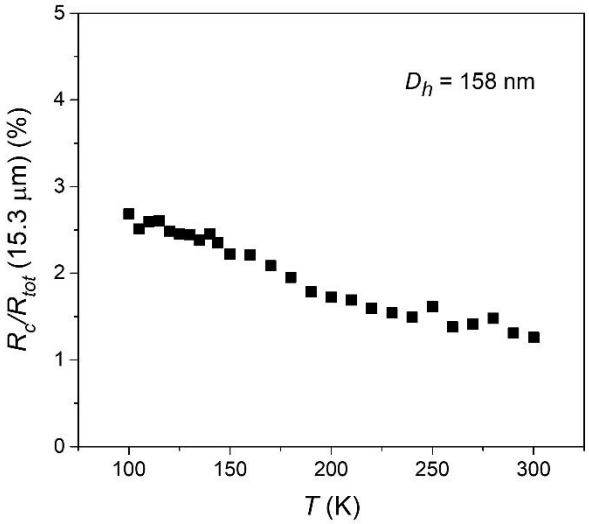

Supplementary Figure 7. Ratio of the contact thermal resistance to the measured total thermal resistance for the 158 nm diameter wire at L = 15.3 μm.

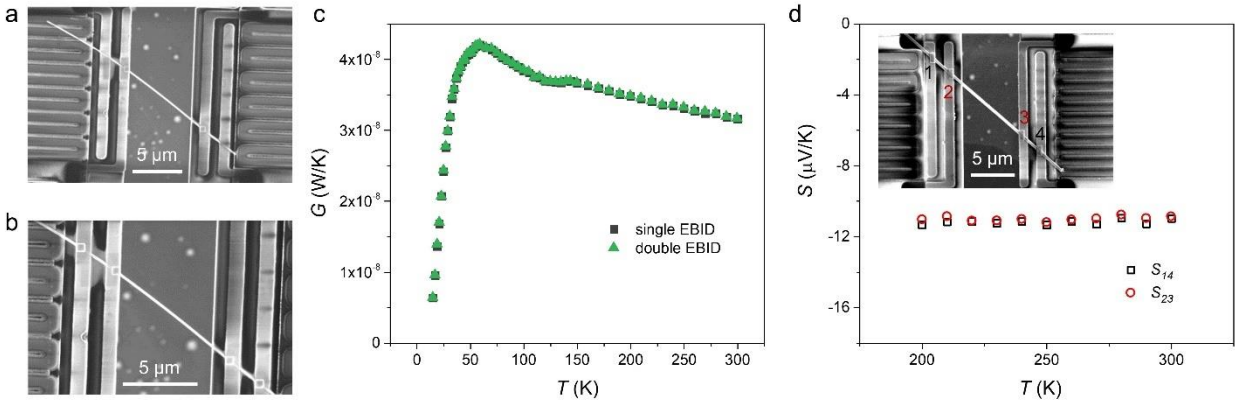

Supplementary Figure 8. SEM micrographs of a $NbSe_3$ nanowire sample with (a) a single EBID treatment, and (b) double EBID treatments. (c) The measured thermal conductance of the nanowire sample after the first and second EBID treatment overlaps with each other, indicating the negligible contact thermal resistance. (d) Measured Seebeck coefficient between the two outer S_{14}, and inner S_{23}, electrodes, respectively. Inset: An SEM micrograph of a 132 nm diameter $NbSe_3$ nanowire placed on the measurement device with EBID of Pt treated at the contacts.

Based on what we have demonstrated in our previous publication[1], which showed that the measured thermal conductance of a $NbSe_3$ wire with a single and double round of EBID treatment overlap with each other (Fig. S8a-c), suggesting that with EBID, the contact thermal resistance is negligible. To further confirm this, we measured the Seebeck coefficients from different sets of electrodes, following the approach developed by Mavrokefalos et al.[13].

As shown in the inset of Fig. S8d, a 132 nm diameter $NbSe_3$ nanowire has been treated with EBID of Pt at the contacts with the underlying electrodes. Through comparing the measured Seebeck coefficients from different pairs of electrodes, we can determine whether the contact thermal resistance is negligible or not. This approach essentially uses the nanowire and the Pt electrodes as a differential thermocouple to determine the temperature drops between the contacts. The Seebeck voltages were measured between both the two inner (2&3) and the two outer (1&4)

electrodes, which would yield different values if the contact thermal resistance were not negligible. Fig. S8d shows that the Seebeck coefficients measured from the two sets of electrodes essentially overlap with each other in the temperature range from 200 – 300 K, which proves that the contact thermal resistance is indeed marginal. In the present work, we have also found that with and without EBID deposition, the obtained thermal conductivity essentially remains the same, indicating that the contact thermal resistance is indeed negligible.

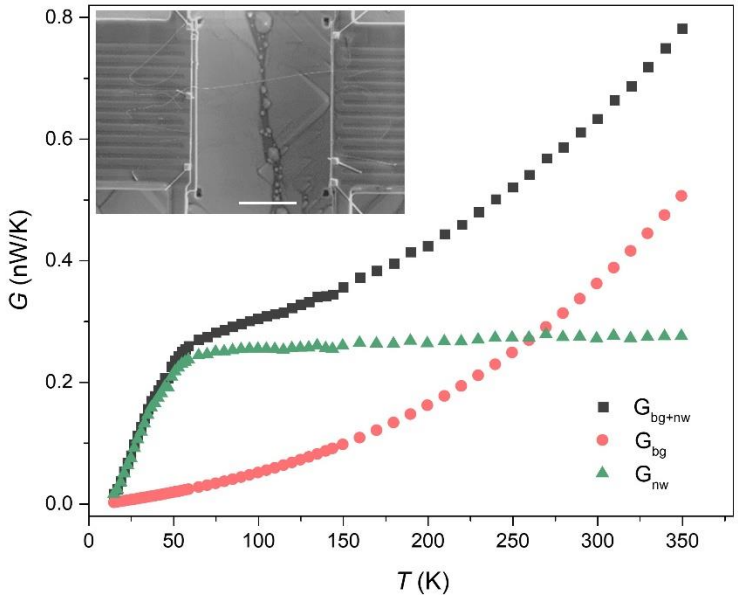

Supplementary Figure 9. Measured total thermal conductance, G_{bg+nw}, background thermal conductance, G_{bg}, and the sample thermal conductance, G_{nw}, for a 13.7 nm thick, 29 nm wide $NbSe_3$ nanowire sample. The inset is the SEM micrograph of the measured sample, where the scale bar is 6 μm.

For very thin $NbSe_3$ nanowires with long suspended length, the intrinsic sample thermal conductance is on the same order of magnitude as the background thermal conductance, G_{bg}, and the background heat transfer effect must be taken into account. To do this, we measured a blank device of identical configuration, and the measured G_{bg} was fitted to a 4^{th} order polynomial function, which was then subtracted from the measured total thermal conductance. Shown in Fig. S9 is the measured total thermal conductance, G_{bg+nw}, background thermal conductance, G_{bg}, and the sample thermal conductance after subtracting the background conductance, G_{nw}, where the measured sample is a 13.7 nm thick, 29 nm wide $NbSe_3$ nanowire. It can be seen that background thermal transport contributes nearly ~65% to the total measured thermal conductance at 350 K, which is likely due to the thermal radiation energy exchange between the two membranes and supporting legs, and its contribution reduces as temperature decreases. We also note that G_{bg} does not show appreciable variation (within ~3%) among devices with the same gap sizes between the two membranes.

Supplementary Note 7. Electronic thermal conductivity

We measured the electrical resistance, R, of individual $NbSe_3$ nanowires using the four-probe approach, and the measurement details have been described in our recently report[1]. To exclude the effects from CDW sliding, we make sure the applied electric field is much smaller than the depinning threshold electrical field, and the obtained I−V curve maintains a linear shape. Fig. S10 shows the temperature dependent electrical resistivity, ρ, obtained based on the measured R and the geometrical information of the nanowire. One can observe a systematic variation for the magnitude and shape of $\rho(T)$ as the wire diameter reduces with two distinct regimes. First for D_h > 30 nm, the $NbSe_3$ nanowires retain a metallic phase, as indicated by the magnitude of the electrical resistivity (ρ(300 K) < 4×10^{-4} Ω cm) and the sign of the $d\rho/dT$. The enhancement of the resistivity in smaller wires could be attributed to stronger scattering of electrons at the nanowire surface. For D_h < 30 nm, the electrical resistivity increases drastically, and the two abnormal peaks corresponding to CDW phase transitions become less distinguishable. As the size reduces to D_h = 10.8 nm, the signatures of CDW phase transition totally disappear, and $\rho(T)$ exhibits a nonmetallic behavior over the entire temperature range.

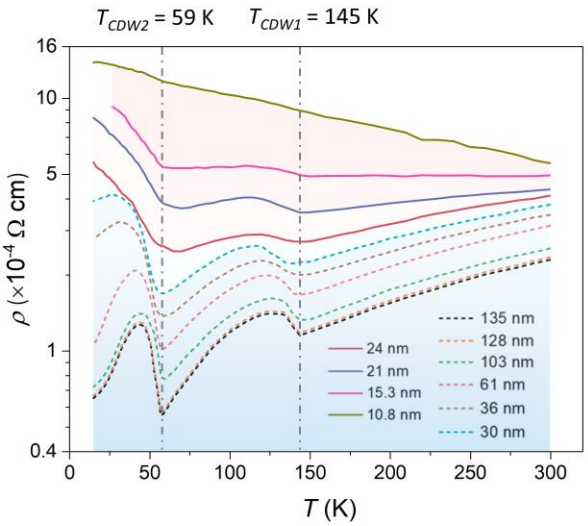

Supplementary Figure 10. Temperature dependent electrical resistivity for $NbSe_3$ nanowires with different hydraulic diameters, where the dashed and solid lines represent two stages of the electrical conduction when the transverse dimension reduces.

The transition from metallic to nonmetallic behavior and the disappearance of resistivity anomalies observed for smaller $NbSe_3$ nanowires are in agreement with that reported previously[14–16]. In bulk $NbSe_3$ crystals, the phase transition is 3D ordering of the CDW fluctuations, with distinct CDW phase-phase correlation length along different crystalline directions. As such, when the crystal thickness becomes much smaller than the CDW's transverse phase correlation length, a stronger surface pinning effect would occur. Based on the calculated R(300 K)/R(10 K) ratio and previous X-ray diffraction measurements[17], we conclude that the phase correlation length along a axis in our $NbSe_3$ nanowires is ~100 nm. Assuming comparable correlation length along a and c[17], for the $NbSe_3$ nanowire of D_h = 24 nm, with the thickness and width measured to be 47 and 16 nm respectively, CDW phase variations along the cross-chain direction would be cut off[18]. As the transverse size further reduces, the stronger surface pinning effects will destroy the long range

coherence along both *a* and *c* directions, which diminishes the transport signatures of CDW phase transitions.

Based on the measured electrical resistivity, ρ, we are able to estimate the electronic thermal conductivity κ_e using the Wiedemann-Franz law as $\kappa_e = LT/\rho$, where L is Lorenz number and the Sommerfeld value of 2.44×10^{-8} $W\Omega K^{-2}$ has been shown to be a good estimation[1], and T is temperature. As shown in Fig. S11a, the estimated κ_e demonstrates a continuously decreasing trend as lateral dimension shrinks. Moreover, different from the wires with hydraulic diameter larger than 24 nm, the electronic thermal conductivity for thinner wires demonstrates a monotonically increasing trend as temperature ramps up, which could be attributed to the diminished electrical resistivity bumps at the two CDW phase transition temperatures shown as in Fig. S10.

The lattice thermal conductivity, κ_l, could then be obtained by subtracting electronic thermal conductivity from the measured total thermal conductivity. Fig. S11b plots the room temperature value of the total, lattice, and electronic thermal conductivity as a function of wire hydraulic diameter. For wires with D_h from 135 to 24 nm, the electronic contribution to the total thermal conductivity is ~40-45%. However, as the lateral dimension further reduces, κ_e drops drastically, and for D_h = 10.8 nm, the electronic contribution is only 3%. As such, the observed increasing κ_t should not come from electronic contribution, but instead, it is mainly phonons that lead to the thermal conductivity escalation by 25-fold at 300 K.

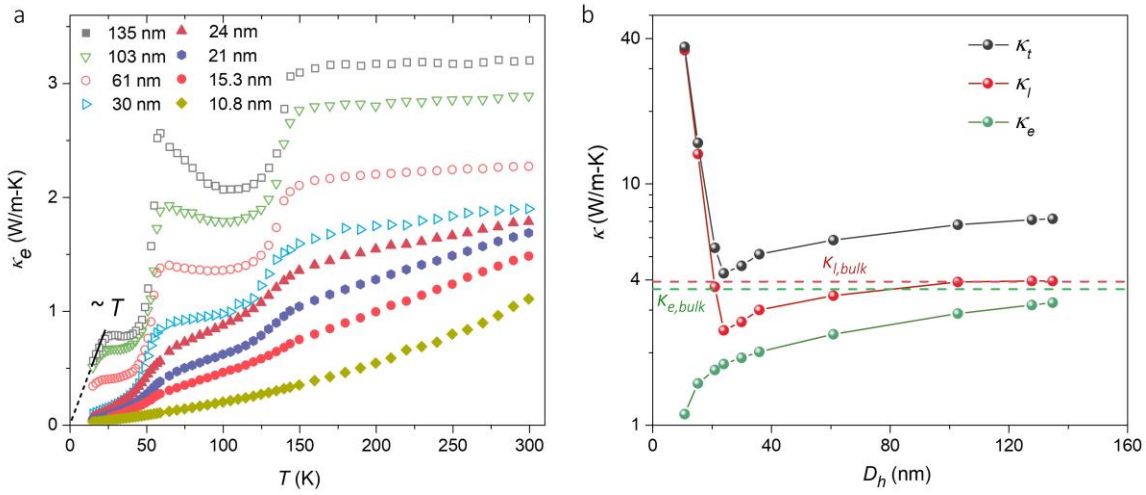

Supplementary Figure 11. (a) Estimated electronic thermal conductivity for $NbSe_3$ nanowires with different lateral dimensions in the temperature range of 15-300 K. (b) Total, lattice, and electronic thermal conductivity for wires with different hydraulic diameters at 300 K.

For the estimation of the percentage contribution of electrons to the thermal conductivity, we used the Wiedemann-Franz law with the Lorenz number taking the Sommerfeld value. As it is calculated based on free electron approximation[19,20], the Sommerfeld value represents an upper limit of the Lorenz number in conventional Fermi Liquid conductors. This has been experimentally verified in different metals, such as Cu[21] and Ni[22], which shows that the Lorenz number is always smaller than the Sommerfeld value. For the Weyl semimetal tungsten diphosphide with strong electron-electron or electron-phonon interaction, although violation of the Wiedemann Franz law occurs due to the hydrodynamic electron flow, the Lorenz number is also much lower than the Sommerfeld value, as shown by Gooth et al.[23]. Therefore, the adoption of the Sommerfeld value

for the Weidemann-Franz can only over-estimate the electronic contribution and we showed that even so, the electronic thermal conductivity is much smaller than the lattice thermal conductivity.

Supplementary Note 8. Divergent thermal transport in ultra-thin $NbSe_3$ nanowires

Based on the observed cross-sectional size dependent thermal conductivity, it will be also interesting to explore the axial thermal conductivity as a function of the sample length. To accomplish this, we have measured the same nanowire with different lengths between the heat source and heat sink through re-suspending the wire multiple times. In order to show the actual suspended length, L, of each measured sample in Fig. 2b, we replot the normalized κ as a function of L in Fig. S12. To ensure a meaningful comparison among samples with different hydraulic diameters, we intentionally kept the maximum length of each measured nanowire to be ~15 μm (14.2–16.3 μm).

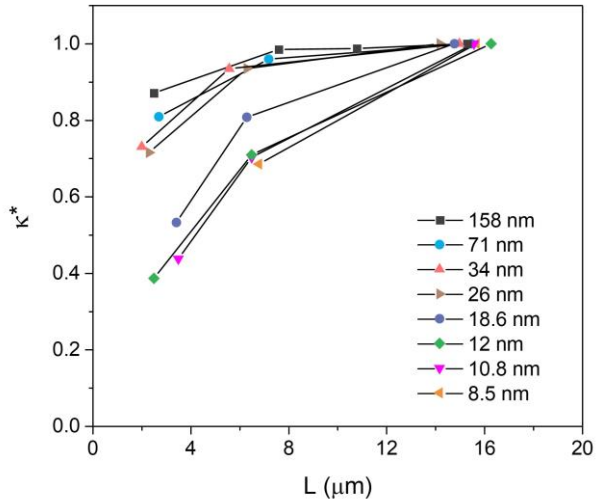

Supplementary Figure 12. Normalized thermal conductivity plotted as a function of the suspended length for $NbSe_3$ nanowires with different hydraulic diameters.

To explore the length dependent thermal transport of ultra-thin $NbSe_3$ nanowires in a much wider length regime, we performed additional measurements for samples with ultra-long suspended length. Fig. S13a shows an example of the measured thin wire with D_h = 12.3 nm, and L = 28.2 μm. In order to rule out any complexity related with different samples, we re-suspended the same nanowire multiple times to microdevices with narrower gap distances. Fig. S13b-c show the 12.3 nm nanowire re-suspended two times with L as 19.1 and 13.5 μm, respectively.

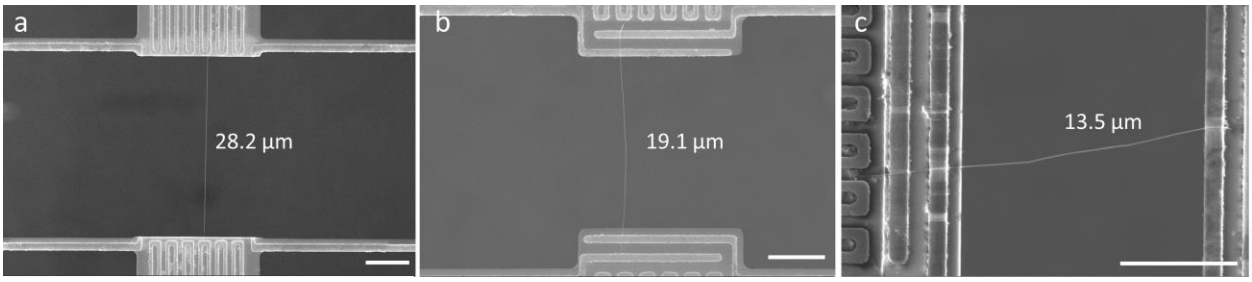

Supplementary Figure 13. (a-c) SEM images of the same $NbSe_3$ nanowire (D_h = 12.3 nm) with different suspended length between heat source and heat sink, where the scale bars are all 6 μm.

The reported work represents the first experimental demonstration of the divergent thermal conductivity for 1D phonons persisting over a distance well beyond the bulk phonon MFP. The early studies on thermal transport through 1D lattices inspired by the pioneering work of Fermi, Pasta, Ulam, and Tsingou (FPUT) focuses on the underlying physics of the recurrence of phonon modes, which leads to divergent thermal conductivity for 1D non-linear lattices with length[24–26]. After a few decades of studies, solitons have been considered to be responsible for the divergent thermal conductivity and significant efforts have been made to explore what conditions are required to eliminate the solitons to render normal thermal conductivity[27–29]. However, there are recent studies indicating that it is low frequency phonons that are responsible for the divergent thermal conductivity in 1D lattices[30]. Since 1990s, efforts have been shifted to study the power law dependence for the thermal conductivity of 1D and 2D systems, and explore what type of interatomic potentials give rise to divergent thermal conductivity[31–36]. In a perspective letter written by Livi and Lepri in 2003[37], two outstanding questions are identified regarding superdiffusive thermal transport of 1D lattices: 1) is there any universal scaling laws describing this anomalous phenomena? and 2) how is it affected by the nature of phonon-phonon scattering (Normal or *Umklapp*)? With subsequent efforts in the past two decades, it is accepted that for a variety of interatomic potentials for 1D lattices, under the long chain limit the thermal conductivity will diverge with length following a 1/3 power law[34–36]; however, there are still some discussions on whether this is a universal law[38].

As to the debate on the exponent, different values have been proposed under different modeling conditions and without experimental data, no consensus has been achieved even though more and more modeling results support the 1/3 power law. For example, the thermal conductivity of FPUT chains was calculated by Lepri et al. in 1998 using mode coupling theory, and the divergent exponent was firstly estimated to be 2/5[31]. However, in 2002, through performing a renormalization-group calculation on the stochastic hydrodynamic equations for a 1D fluid, Narayan et al. claimed that the divergent exponent should be 1/3 as a result of momentum conservation in the 1D systems[32]. Moreover, they pointed out that the 2/5 divergence is obtained due to the incorrect scaling conversion adopted by previous studies[32]. Only after one year, through numerically simulating 1D lattices with different lengths, Lepri et al. demonstrated that instead of showing the expected value of 1/3, their results are closer to 2/5 power law divergence, in agreement with the mode coupling prediction, although the physical origin was still unclear[33]. Later, the 2/5 divergence was also derived both from a kinetic theory calculation[39] and equilibrium as well as nonequilibrium molecular dynamics simulation[34,36]. It has been conjectured that the 2/5 exponent is for systems with purely longitudinal dynamics (FPUT model without transverse motion), while a crossover towards 1/3 is to be expected in the presence of coupling to transverse motions and/or in the long length limit[34–36].

We conclude that our data support the 1/3 power law dependence because 1) the existence of transverse motions and 2) our chain length is really in the long-chain limit. In theoretical studies, numerical simulations and mode coupling analyses have predicted a $\kappa \propto L^{2/5}$ divergence law for 1D nonlinear lattices when the transverse motion can be neglected[31,34,36]. For the case with intermediate transverse motions for 1D phonons, $\kappa \propto L^{1/3}$ dependence is expected[34,36]. Moreover, it has been shown that the 2/5 power law dependence would eventually crossover to 1/3 at long length scales, and it has been suggested that $\kappa \propto L^{1/3}$ power law divergence should be a generic feature for models with momentum conservation and transverse motions at long length limit[34–36]. In reality the atoms in the $NbSe_3$ chains should have transverse motion and our chain length is well beyond the N > 10,000 requirements for long chain limit, which leads to the observed 1/3 power law length dependence for ultra-thin nanowires.

Supplementary Note 9. Young's modulus measurements

To measure the Young's modulus, individual $NbSe_3$ nanowires were transferred to an 8 μm wide Si trench using an in-house built micromanipulator. A layer of Pt/C composite was locally deposited at the two ends of the nanowire through EBID to clamp the ribbon to the substrate (Fig. S14). We then performed the three-point bending test using an atomic force microscope (AFM, Bruker Dimension Icon). Before each measurement, we first calibrated the deflection sensitivity of the cantilever by tapping it on the hard Si substrate in the contact mode. Then, the probe was withdrawn from the surface, and the spring constant was extracted through a thermal tune process during its self-excitation under ambient conditions[40,41].

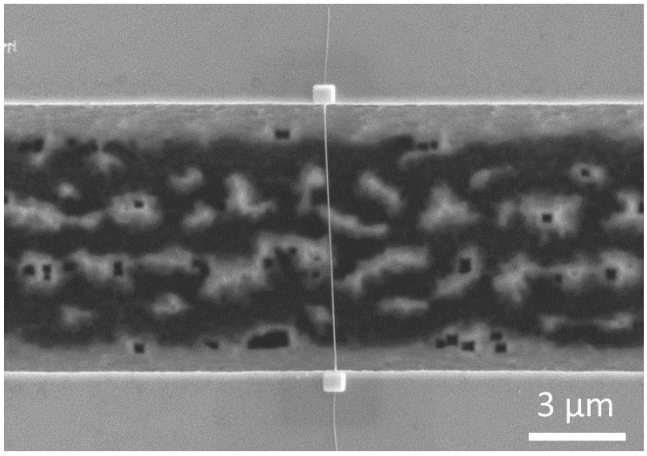

Supplementary Figure 14. An SEM micrograph showing a $NbSe_3$ nanowire transferred to bridge a Si trench.

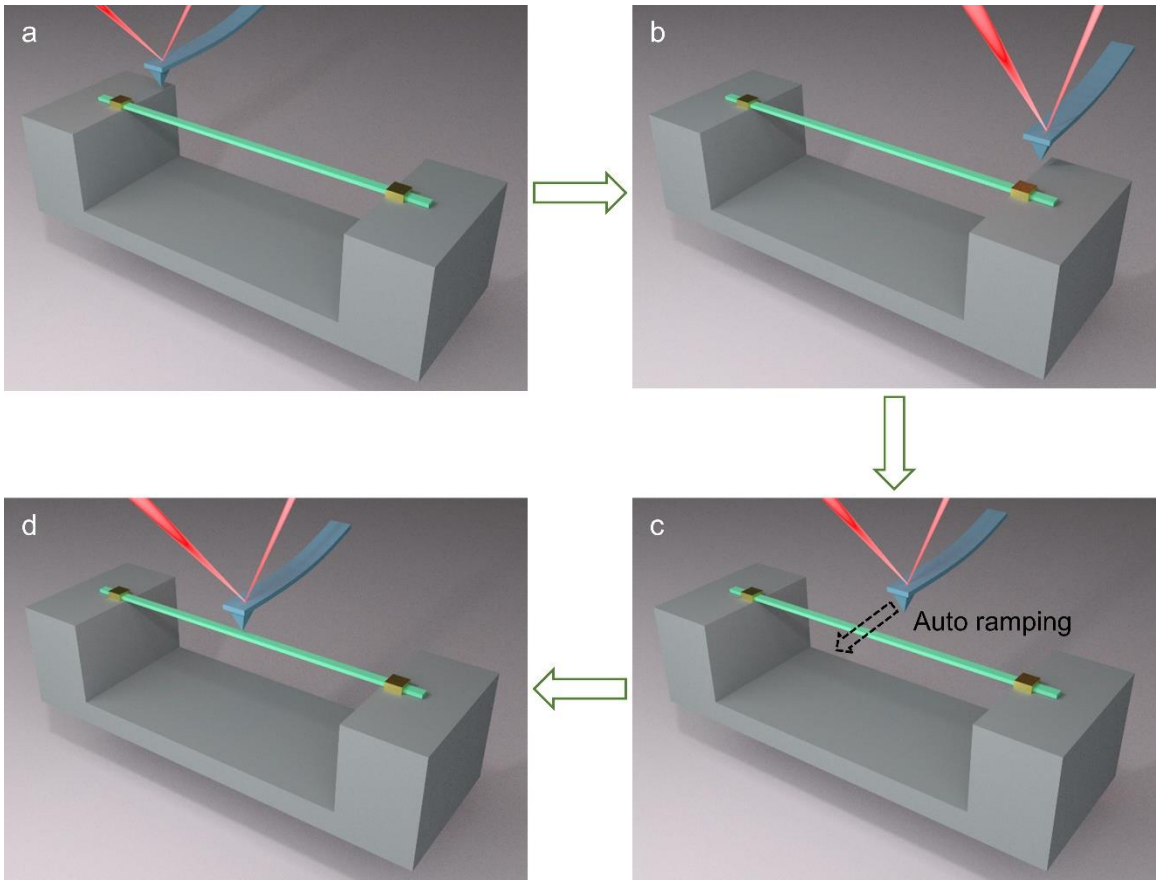

Supplementary Figure 15. Schematic diagrams showing the procedures for the three-point bending test using AFM tip. (a-b) AFM tip ramping to determine the locations for the two edges of the Si trench. (c) Locate the AFM tip right at the middle of the trench by assigning the location in the coordinates. Use auto ramping function to move the AFM tip toward the nanowire. (d) Locate the AFM tip at the middle point of the nanowire and perform the bending test.

Fig. S15 shows the procedures we take to accurately locate the AFM tip on top of the middle point of the nanowire. First, to determine the middle point of the trench, we tapped the AFM tip near the edge of the Si trench to accurately obtain the location of the two edges of the trench. Then, the AFM tip was moved to the middle point by assigning the location in the coordinates. After this, the AFM underwent an auto ramping process with a step size of 20 nm using the NanoScope software (Bruker) along the direction perpendicular to the nanowire axial direction. After the location of the nanowire was determined, we then performed the bending test.

The bending test was performed by pushing the middle point of the nanowire using the AFM cantilever. To obtain the nanowire displacement, d, we use the relationship of $d = Z - \Delta Z_c$, where Z is the total displacement of the AFM cantilever, and ΔZ_c is the tip deflection. ΔZ_c is obtained by applying the Hook's law as $F = \Delta Z_c k$, where F is the measured force and k is the spring constant of the cantilever. Therefore, a single measurement yields the F-D curve for the examined $NbSe_3$ nanowire. From Fig. 3a in the main manuscript, it can be seen that the F-D curves recorded at the extension and retraction process overlap perfectly with each other, indicating that the nanowires are firmly anchored. Moreover, the bending tests were repeated three times for each sample with

reproducible results, showing the rigidity of the constraints and the elastic nature of the nanowires within the measured range.

Fig. S16 plots the measured F-D curve for a representative $NbSe_3$ nanowire, where the black curve is recorded during the extension process whereas the blue curve is the retraction data. To extract the Young's modulus for the measured sample, we apply the model put forward by Yaish et al.[42]:

$$F = \frac{192EI}{L^3} d(L/2) f(\alpha), \tag{S8}$$

where E is the Young's modulus, I is the area moment of inertia, L is the suspended length of the nanowire, and $d(L/2)$ is the vertical deflection at the middle point of the wire. Note that we approximate the cross-section of the $NbSe_3$ nanowires to be rectangular to calculate the area moment of inertia. $\alpha = L^2T/EI$ (T is the overall tension along the wire), and α measures the ratio between the stretching and bending contributions to the beam deflection. In fact, if the cross-section deviates from rectangular shape, the above assumption will only underestimate the Young's modulus.

We note that Eq. (S8) yields the well-known linear beam deflection approximation in the case of $f(\alpha) = 1$. However, this relationship is only valid when the wire deflections are smaller than its thickness and is also very sensitive to initial stress. For deflections greater or comparable to the beam thickness, which is the case for our ultra-thin $NbSe_3$ nanowires, the tensile forces due to stretching become significant, and the F-D deviates substantially from the linear relation. As shown by Yaish et al., for deflections up to 10 times of the nanowire thickness, $f(\alpha)$ could be approximated by[42]:

$$f_{app}\left(\alpha_{app}\right) = 1 + 2.412\times10^{-2}\alpha_{app} - 1.407\times10^{-6}{\alpha_{app}}^2, \tag{S9}$$

where

$$\alpha_{app} = \frac{L^2T_0}{EI} + \frac{6\varepsilon(140+\varepsilon)}{350+3\varepsilon}. \tag{S10}$$

Here, T_0 is the residual or initial tension, and $\varepsilon = u(L/2)^2S/I$, where S is the cross-sectional area. As such, for a given set of F-D data, Eq. S8 and S10 can be solved self-consistently, which will give the two unknowns, E and T_0.

The red curve shown in Fig. S16 is the fitted data using the model described above, where the width of the nanowire is measured from the SEM micrograph and the thickness is obtained by AFM scanning. For this nanowire with width of 57 nm and thickness of 13.5 nm, the Young's modulus is determined to be 169 GPa. In order to compare the measured Young's modulus of thin nanowires to that of bulk $NbSe_3$, $NbSe_3$ nanowires with larger lateral dimensions were also measured. As shown in Fig. 3b in the main paper, the measured E of $NbSe_3$ nanowires with D_h larger than 40 nm is close to a constant, and the averaged bulk value is ~ 86 GPa. It is important to note that this measured bulk data is in agreement with the previously measured result of 150 ± 100 GPa on bulk $NbSe_3$[43,44].

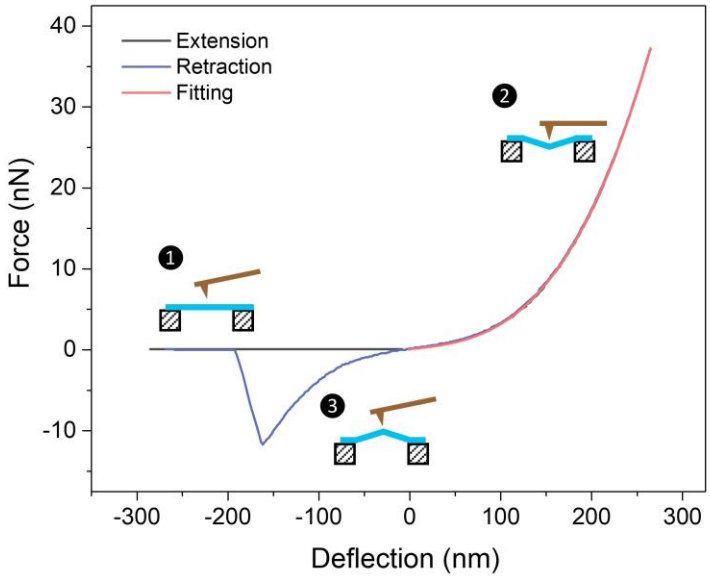

Supplementary Figure 16. Force-deflection curved recorded during the three-point bending test for the 21.8 nm $NbSe_3$ nanowire, where the fitted curve is also plotted for comparison.

Supplementary Table 2. Summary of the cross-section dimension, suspended length and measured Young's modulus of $NbSe_3$ nanowires.

Sample ID	Width (nm)	Thickness (nm)	Hydraulic diameter (nm)	Sample length (μm)	*E* (GPa)
#1	212	104	139.5	8.9	71.3
#2	171	72	101.3	9.3	96.3
#3	193	52	81.9	8.6	82
#4	103	64	78.9	8.7	77.5
#5	78	42	54.6	8.5	94
#6	116	33	51.4	8.3	80.9
#7	56	31	39.9	8.2	102
#8	102	18.2	30.9	8.7	112.1
#9	37	21.3	27.0	8.4	110.2
#10	47	16.5	24.4	8.6	147.5
#11	33	17	22.4	8.7	144.3
#12	57	13.5	21.8	8.4	169.4
#13	30	14	19.1	8.4	191
#14	38	12.6	18.9	8.3	215
#15	31	12.4	17.7	8.2	183

#16	27	11	15.6	8.3	229
#17	19	10.5	13.5	8.4	315.9
#18	17	10.8	13.2	8.5	276
#19	13	11.7	12.3	8.4	393
#20	16	7.1	9.8	8.4	423
#21	15	5.7	8.3	8.3	489

Supplementary Note 10. Modeling thermal conductivity considering elastic stiffening effects

To understand the effects of elastic stiffening on thermal transport in $NbSe_3$, we calculate bulk phonon dispersion relations considering different interatomic force constants. Similar to our previous work[1], the Vienna *ab initio* simulation package (VASP) is prepared for the density function theory (DFT) calculation for the interatomic force constants[45]. An energy cut-off of 280 eV is chosen for the plane wave basis sets in the projector augmented wave (PAW) method. The exchange correlation interaction is treated with the general gradient approximation (GGA) in the Perdew-Burke-Ernzerhof (PBE) parametrization[46]. A 2×3×2 supercell is employed for the second-order and third-order calculations. The second order IFCs (inter-atomic force constants) of each atomic structure are obtained using density functional perturbation theory (DFPT)[47] and the phonopy code[48]. Only interactions up to the second nearest neighbors are considered in the third-order calculations. Based on the DFT result, the phonon dispersion (Fig. S17) can be obtained by solving the phonon BTE as implemented in the ShengBTE code[49]. The lattice thermal conductivity along the molecular chain direction can then be obtained under the framework of the Boltzmann Transport Equation (BTE) as[46,49]

$$\kappa_l = \frac{1}{k_B T^2 \Omega N} \sum_j f_0 \left(f_0 + 1 \right) \left(\hbar \omega \upsilon_j \right)^2 \tau_j , \tag{S11}$$

where k_B, T, Ω, N, $\hbar$, ω, and υ_j are the Boltzmann constant, temperature, volume of unit cell, number of wave vector points, reduced Plank constant, phonon frequency and mode j dependent phonon group velocity, respectively. f_0 is the equilibrium Bose-Einstein distribution, and τ_j is the mode dependent phonon relaxation time.

The calculated phonon dispersion relations along high symmetry reciprocal points is shown in Fig. S17. The increased interatomic force constant has profound impacts on the phonon band structure. It can be seen that the maximum frequency increases for the acoustic phonon modes along molecular chain direction (Γ-Z), which leads to phonon stiffening effect, and higher phonon group velocity for the acoustic modes. Meanwhile, the phonon relaxation time increases drastically (Fig. 3d in main paper) owing to the reduced phase space available for phonon-phonon scattering. We plotted the calculated room temperature thermal conductivity as a function of force constant ratio with respect to the bulk value in Fig. 3c. It can be seen that κ_l increases sharply as the force constant increases. At the original bulk force constant value, the calculated room temperature κ is 7.1 W/m-K, and increases to 106.8 W/m-K as the force constant ratio escalates to 6.

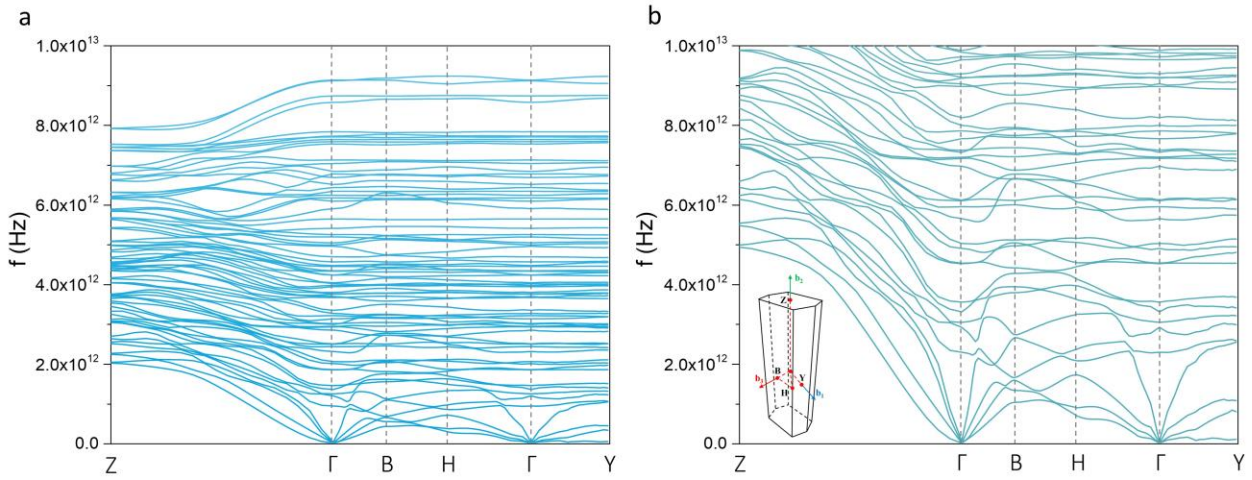

Supplementary Figure 17. Calculated phonon dispersion relation for bulk $NbSe_3$ with interatomic force constant ratio with respect to the original bulk value as (a) 1, and (b) 6.

According to the calculated phonon dispersion relation, the maximum acoustic phonon frequencies increase due to the elastic stiffening effect. As shown in Fig. S17b, the maximum frequency, f_c, of cross-chain acoustic phonon (along Γ-B direction) is ~1.5 THz. If we consider the relation of $f_c = k_B T/2\pi\hbar$, where k_B and $\hbar$ are Boltzmann constant and reduced Planck constant, respectively, this cut-off frequency indicates most of the cross-chain phonon modes are activated as T increases to 72 K. In contrast, f_c of acoustic phonons along the molecular chain direction (Γ-Z) is ~6.5 THz, suggesting that along chain 1D acoustic phonons are continuously activated as T ramps up to until 312 K. We believe this explains the observed linear T dependence of measured κ of the ultra-thin $NbSe_3$ nanowires at high T regime (Fig. 2d). Note that in our calculations, we enhance the bonding strengths for both intra-chain and inter-chain interactions, while in reality it is more likely that only intra-chain strength is enhanced. It is important to point out that without the enhancement of inter-chain force constants, the effects of 1D along chain phonons will only be more significant. In fact, if we only enhance the force constant along the molecular chain direction, the calculated thermal conductivity diverges as we increase the density of grids along the molecular chain direction.

As shown in Fig. S18, we also calculate the thermal conductivity accumulation as a function of phonon frequency with different interatomic force constant ratios. It can be seen that the contributions from phonons with higher frequencies increase as the force constant increases. For $NbSe_3$ with the original force constant value, phonons with frequencies less than 3.9 THz contributes to 90% of thermal transport; however, this value increases to 7.8 THz as the force constant ratio increases to 6. This indicates that elastic stiffening leads to a greater portion of along-chain phonons with higher frequencies contributing to thermal transport in $NbSe_3$.

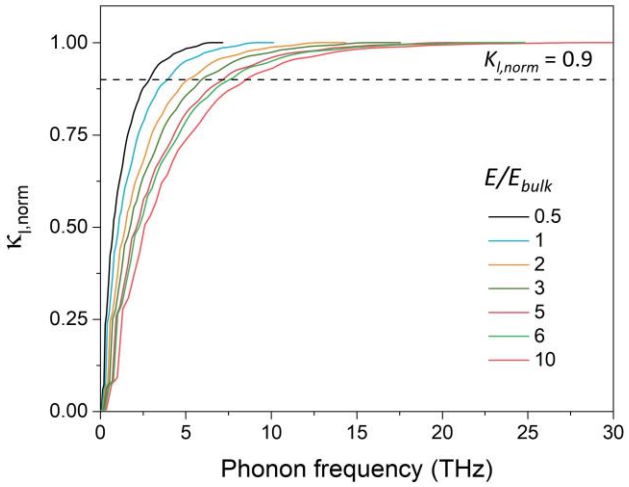

Supplementary Figure 18. Normalized room temperature thermal conductivity accumulation function with respect to the phonon frequency of bulk $NbSe_3$.

To explore how elastic stiffening affects phonon scattering processes in $NbSe_3$ nanowires, we separately calculated the Normal and *Umklapp* scattering rates as the interatomic force constant increases. Here, the Normal and *Umklapp* scattering rates are calculated considering the conservation of momentum as $q'' = q \pm q'$ and the conservation of quasi-momentum as $q" = q \pm q' + G$ respectively, where q, $q'$and q'' represent the wave vectors of phonons experiencing three-phonon scattering and G represents the reciprocal-lattice vector. Both scattering processes satisfy the conservation of energy, namely $\hbar\omega_q + \hbar\omega_{q'} = \hbar\omega_{q''}$ for absorption process and $\hbar\omega_q = \hbar\omega_{q'} + \hbar\omega_{q''}$ for emission process, where ω_q denotes the angular frequency of phonon mode q. Fig. 3d in the main paper shows that as the Young's modulus ratio increases to 6, Normal scattering rate becomes nearly one order of magnitude stronger than the *Umklapp* Scattering. Fig. 3e shows the calculated ratio of phonon mode dependent *Umklapp* over Normal scattering rates for Young's modulus ratios of 1 and 6, respectively, from which we can clearly see that Normal scattering becomes more important due to elastic stiffening, which indicates that the dominant phonon scattering mechanism is the momentum conserved Normal scattering.

To confirm that similar to the FPUT model lattices, the anomalous superdiffusive thermal transport in the ultra-thin $NbSe_3$ nanowires emerges due to the remaining anharmonicity. We extracted the anharmonic inter-atomic interactions from our DFT calculations and conducted the numerical modeling using the molecular dynamics (MD) simulation with the LAMMPS package[50]. We considered the α-FPUT model in our simulation, which takes into account the second-order and third-order interaction potentials as follows[51]:

$$V(z) = \frac{k}{2}Z^2 + \frac{\alpha}{3}Z^3. \tag{S12}$$

We note that the α-FPUT model is consistent with our DFT calculations, as they both consider the second-order and third-order force constants. In the DFT calculation for the inter-atomic force constant, the total potential energy of the system can be expanded into[49]:

$$E = E_0 + \frac{1}{2}\Phi_{ij}^{uv} r_i^u i_j^v + \frac{1}{3!}\Phi_{ijk}^{uvw} r_i^u i_j^v i_k^w. \tag{S13}$$

Here, the coefficients Φ in the *n*-th order term are the corresponding *n*-th order force constant, and the subscripts *i, j, k* represents three different atoms and the superscripts *u, v, w* are the vibration directions of each atom. The parameters in the interaction potentials of α-FPUT model are derived through averaging the second-order and third-order force constants of ultra-thin $NbSe_3$ nanowires with $E/E_{bulk} = 6$, which can be described as:

$$k = \frac{\sum_{i\neq j}^{u=v} \Phi_{ij}^{uv}}{2N_2}, \tag{S14}$$

$$\alpha = \frac{\sum_{i\neq j\ or\ j\neq k\ or\ i\neq k}^{u=v=w} \Phi_{ijk}^{uvw}}{4N_3}. \tag{S15}$$

Here N_2 and N_3 are the total number of second-order and third-order force constants. We divide the force constants by 2 because in FPUT model, the interaction potential for each atom must be counted twice to consider their two neighbor atoms. The equilibrium distance in the α-FPUT model is set as the bond length of the $NbSe_3$ $(2.67A)^2$.

During the MD simulation, the velocity Verlet algorithm with a time step of 1 fs is used for the integration of the motion equations[52]. The system is first equilibrated at 300 K for 1 ns. After the system reaches thermal equilibrium, the temperature of the heat source and heat sink regions are set to 400 K and 200 K, respectively. The large temperature difference is used to guarantee a stable temperature gradient, *dT/dZ*, during the thermal equilibrium process. Each simulation run is carried out with an equilibrium time of 5 ns~50 ns to ensure that the system reaches steady state, and the exact equilibrium time depends on the size of the system. The thermal conductivity of the FPUT model can then be calculated as

$$\kappa = \frac{q}{A\frac{dT}{dZ}}, \tag{S16}$$

where *q* is the heat flux, *A* is the effective cross-section of the corresponding FPUT model, which is the same as the effective cross-section of a single $NbSe_3$ molecular chain.

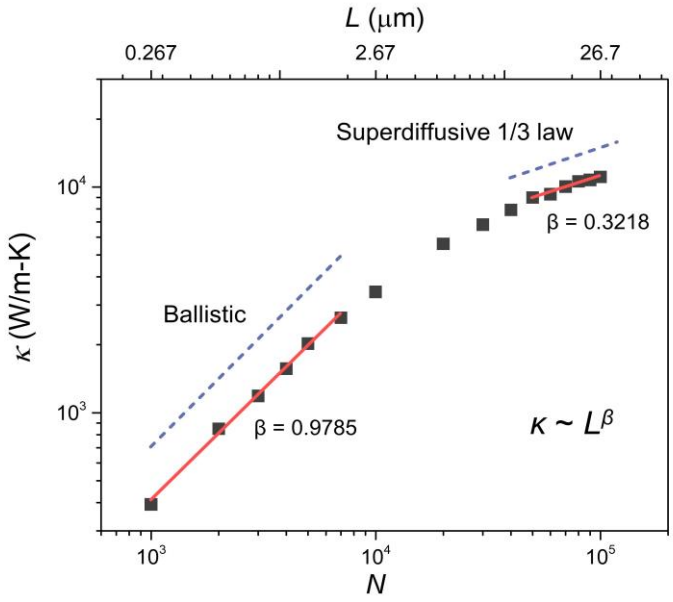

Supplementary Figure 19. Modeled length dependent thermal conductivity of a FPUT-like $NbSe_3$ single molecular chain at 300 K, where different thermal transport mechanism are labeled in respective length regimes.

The calculated thermal conductivity in the length regime of N from 1,000 to 100,000 are shown in Fig. S19. It can be seen that for N < 10,000, the obtained κ displays a nearly linear relationship with chain length, suggesting ballistic transport in this short length regime. This indicates that the phonon mean free path is larger than the chain length, and the system behaves like a harmonic system. As the chain length increases beyond 50,000, a 1/3 power law dependence can be clearly discerned, showcasing the superdiffusive thermal transport phenomena. It is worth noting that the much sharper length dependence for N < 30,000 (corresponding to length of 8.01 μm) and subsequent 1/3 power law divergence resembles our experimental observation for the ultra-thin $NbSe_3$ nanowires in Fig. 2c. Our results are consistent with the previous work on FPUT models, showing that for nonlinear 1D lattice with transverse motions, a 1/3 power dependence is expected at long chain limit[34–36]. This in turn proves that similar to the FPUT model lattices, the anomalous superdiffusive thermal transport in the ultra-thin $NbSe_3$ nanowires emerges due to the remaining anharmonicity.

References:

1. Yang, L. *et al.* Distinct Signatures of Electron–Phonon Coupling Observed in the Lattice Thermal Conductivity of NbSe3 Nanowires. *Nano Lett.* **19**, 415–421 (2019).
2. Hodeau, J. L. *et al.* Charge-density waves in NbSe3 at 145K: crystal structures and electron diffraction studies. *J. Phys. C Solid State Phys.* **11**, 4117–4130 (1978).
3. Zhang, Q. *et al.* Thermal transport in quasi-1D van der Waals crystal Ta2Pd3Se8 nanowires: size and length dependence. *ACS Nano* **12**, 2634–2642 (2018).
4. Yang, L. Phonon Transport in Nanowires–Beyond Classical Size Effects. *Ph.D. thesis, Vanderbilt Univ.* (2019).
5. Shi, L. *et al.* Measuring thermal and thermoelectric properties of one-dimensional nanostructures using a microfabricated device. *J. Heat Transfer* **125**, 881 (2003).
6. Wingert, M. C., Chen, Z. C. Y., Kwon, S., Xiang, J. & Chen, R. Ultra-sensitive thermal conductance measurement of one-dimensional nanostructures enhanced by differential bridge. *Rev. Sci. Instrum.* **83**, 024901 (2012).
7. Qian Zhang. Thermal transport in individual nanowires of fine structures. *Ph.D. thesis, Vanderbilt Univ.* (2017).
8. Bi, K. *et al.* Iodine doping effects on the lattice thermal conductivity of oxidized polyacetylene nanofibers. *J. Appl. Phys.* **114**, 194302 (2013).
9. Yang, J. *et al.* Enhanced and switchable nanoscale thermal conduction due to van der Waals interfaces. *Nat. Nanotechnol.* **7**, 91–95 (2011).
10. Yang, L. *et al.* Thermal conductivity of individual silicon nanoribbons. *Nanoscale* **8**, 17895–17901 (2016).
11. Yu, C. *et al.* Thermal Contact Resistance and Thermal Conductivity of a Carbon Nanofiber. *J. Heat Transfer* **128**, 234 (2006).
12. Yang, J. *et al.* Measurement of the intrinsic thermal conductivity of a multiwalled carbon nanotube and its contact thermal resistance with the substrate. *Small* **7**, 2334–2340 (2011).
13. Mavrokefalos, A., Pettes, M. T., Zhou, F. & Shi, L. Four-probe measurements of the in-plane thermoelectric properties of nanofilms. *Rev. Sci. Instrum.* **78**, 034901 (2007).
14. Zaitsev-Zotov, S. V. Transport properties of TaS3 and NbSe3 crystals of nanometer-scale transverse dimensions. *Microelectron. Eng.* **69**, 549–554 (2003).
15. Zaitsev-Zotov, S. V. One-dimensionality effects in quasi-one-dimensional conductors. *J. Exp. Theor. Phys. Lett.* **80**, 445–454 (2004).
16. Slot, E., Holst, M. A., Van Der Zant, H. S. J. & Zaitsev-Zotov, S. V. One-dimensional conduction in charge-density-wave nanowires. *Phys. Rev. Lett.* **93**, 176602 (2004).
17. Sweetland, E., Tsai, C.-Y., Wintner, B. A., Brock, J. D. & Thorne, R. E. Measurement of the charge-density-wave correlation length in NbSe3 by high-resolution x-ray scattering. *Phys. Rev. Lett.* **65**, 3165–3168 (1990).
18. McCarten, J., Maher, M., Adelman, T. L. & Thorne., R. E. Size effects and charge-density-wave pinning in NbSe3. *Phys. Rev. Lett.* **63**, 2841–2844 (1989).
19. Sommerfeld, V. A. DIE NATURWISSENSCHAFTEN Zur Elektronentheorie der Metalle. *Naturwissenschaften* **15**, (1927).
20. Kim, H. S., Gibbs, Z. M., Tang, Y., Wang, H. & Snyder, G. J. Characterization of Lorenz number with Seebeck coefficient measurement. *APL Mater.* **3**, 041506 (2015).
21. Zhang, Y. *et al. Determining the Wiedemann-Franz Ratio from the Thermal Hall Conductivity: Application to Cu and YBa 2 Cu 3 O 6.95*. (2000).
22. Onose, Y., Shiomi, Y. & Tokura, Y. Lorenz number determination of the dissipationless

nature of the anomalous hall effect in itinerant ferromagnets. *Phys. Rev. Lett.* **100**, (2008).
23. Gooth, J. *et al.* Thermal and electrical signatures of a hydrodynamic electron fluid in tungsten diphosphide. *Nat. Commun.* **9**, 1–8 (2018).
24. E. Fermi, J. Pasta, and S. Ulam, Los Alamos Science Laboratory Report No. LA1940, 1955.
25. Livi, R., Pettini, M., Ruffo, S., Sparpaglione, M. & Vulpiani, A. Equipartition threshold in nonlinear large Hamiltonian systems: The Fermi-Pasta-Ulam model. *Phys. Rev. A* **31**, 1039–1045 (1985).
26. Toda, M. Studies of a non-linear lattice. *Physics Reports* **18**, 1–123 (1975).
27. Zabusky, N. J. Solitons and energy transport in nonlinear lattices. *Comput. Phys. Commun.* **5**, 1–10 (1973).
28. Toda, M. Solitons and heat conduction. *Phys. Scr.* **20**, 424–430 (1979).
29. Ford, J. The Fermi-Pasta-Ulam problem: Paradox turns discovery. *Physics Reports* **213**, 271–310 (1992).
30. Li, N., Li, B. & Flach, S. Energy carriers in the fermi-pasta-ulam β lattice: Solitons or phonons? *Phys. Rev. Lett.* **105**, 054102 (2010).
31. Lepri, S., Livi, R. & Politi, A. On the anomalous thermal conductivity of one-dimensional lattices. *Europhys. Lett.* **43**, 271–276 (1998).
32. Narayan, O. & Ramaswamy, S. Anomalous Heat Conduction in One-Dimensional Momentum-Conserving Systems. *Phys. Rev. Lett.* **89**, 200601 (2002).
33. Lepri, S., Livi, R. & Politi, A. Universality of anomalous one-dimensional heat conductivity. *Phys. Rev. E - Stat. Physics, Plasmas, Fluids, Relat. Interdiscip. Top.* **68**, 8–11 (2003).
34. Wang, J. S. & Li, B. Intriguing Heat Conduction of a Chain with Transverse Motions. *Phys. Rev. Lett.* **92**, 074302 (2004).
35. Liu, S., Xu, X. F., Xie, R. G., Zhang, G. & Li, B. W. Anomalous heat conduction and anomalous diffusion in low dimensional nanoscale systems. *Eur. Phys. J. B* **85**, 337 (2012).
36. Wang, J. S. & Li, B. Mode-coupling theory and molecular dynamics simulation for heat conduction in a chain with transverse motions. *Phys. Rev. E - Stat. Physics, Plasmas, Fluids, Relat. Interdiscip. Top.* **70**, 16 (2004).
37. Livi, R. & Lepri, S. Thermal physics: Heat in one dimension. *Nature* **421**, 327 (2003).
38. Zhang, Z. *et al.* Size-dependent phononic thermal transport in low-dimensional nanomaterials. *Phys. Rep.* **860**, 1–26 (2020).
39. Pereverzev, A. Fermi-Pasta-Ulam [Formula presented] lattice: Peierls equation and anomalous heat conductivity. *Phys. Rev. E - Stat. Physics, Plasmas, Fluids, Relat. Interdiscip. Top.* **68**, 056124 (2003).
40. Lévy, R. & Maaloum, M. Measuring the spring constant of atomic force microscope cantilevers: Thermal fluctuations and other methods. *Nanotechnology* **13**, 33–37 (2002).
41. Determine Cantilever Spring Constant by Thermal Tune. Available at: http://nanophys.kth.se/nanophys/facilities/nfl/afm/icon/bruker-help/Content/Probe and Sample Guide/ThermalTune/ThermalTune.htm. (Accessed: 1st September 2020)
42. Calahorra, Y., Shtempluck, O., Kotchetkov, V. & Yaish, Y. E. Young's modulus, residual stress, and crystal orientation of doubly clamped silicon nanowire beams. *Nano Lett.* **15**, 2945–2950 (2015).
43. Brill, J. W. & Ong, N. P. Young's modulus of NbSe3. *Solid State Commun.* **25**, 1075–

1078 (1978).
44. Requardt, H., Lorenzo, J. E., Monceau, P., Currat, R. & Krisch, M. Dynamics in the charge-density-wave system NbSe3 using inelastic x-ray scattering with meV energy resolution. *Phys. Rev. B* **66**, 214303 (2002).
45. Kresse, G. & Furthmüller, J. Efficiency of ab-initio total energy calculations for metals and semiconductors using a plane-wave basis set. *Comput. Mater. Sci.* **6**, 15–50 (1996).
46. Kresse, G. & Joubert, D. From ultrasoft pseudopotentials to the projector augmented-wave method. *Phys. Rev. B* **59**, 1758–1775 (1999).
47. Gonze, X. & Lee, C. Dynamical matrices, Born effective charges, dielectric permittivity tensors, and interatomic force constants from density-functional perturbation theory. *Phys. Rev. B* **55**, 10355–10368 (1997).
48. Togo, A., Oba, F. & Tanaka, I. First-principles calculations of the ferroelastic transition between rutile-type and CaCl2-type SiO2 at high pressures. *Phys. Rev. B* **78**, 134106 (2008).
49. Li, W., Carrete, J., A. Katcho, N. & Mingo, N. ShengBTE: A solver of the Boltzmann transport equation for phonons. *Comput. Phys. Commun.* **185**, 1747–1758 (2014).
50. Plimpton, S. Fast parallel algorithms for short-range molecular dynamics. *J. Comput. Phys.* **117**, 1–19 (1995).
51. Lepri, S., Livi, R. & Politi, A. Studies of thermal conductivity in Fermi-Pasta-Ulam-like lattices. *Chaos* **15**, 015118 (2005).
52. Frenkel, D. & Smit, B. *Understanding molecular simulation: From algorithms to applications*. (Academic Press, 2001).